

Sequential tunneling in doped superlattices: Fingerprints of impurity bands and photon-assisted tunneling

Andreas Wacker and Antti-Pekka Jauho

Mikroelektronik Centret, Danmarks Tekniske Universitet, DK-2800 Lyngby, Denmark

Stefan Zeuner* and S. James Allen

Center for Terahertz Science and Technology, University of California at Santa Barbara, Santa Barbara, California 93106

(To appear in Physical Review B, 15. November 1997)

We report a combined theoretical and experimental study of electrical transport in weakly-coupled doped superlattices. Our calculations exhibit negative differential conductivity at sufficiently high electric fields for all dopings. In low-doped samples the presence of impurity bands modifies the current-voltage characteristics substantially and we find two different current peaks whose relative height is changing with the electron temperature. These findings can explain the observation of different peaks in the current-voltage characteristics with and without external THz irradiation in low-doped samples. From our microscopic transport model we obtain quantitative agreement with the experimental current-voltage characteristics without using any fitting parameters. Both our experimental data and our theory show that absolute negative conductance persists over a wide range of frequencies of the free-electron laser source.

72.20.Ht,73.20.Dx,73.40.Gk

I. INTRODUCTION

Perpendicular charge transport in biased superlattices is dominated by resonances due to the alignment of energy levels in different wells. These resonances yield distinct peaks in the current-voltage characteristics [1,2] associated with negative differential conductivity (NDC) at fields above the peak. The instability associated with NDC causes the formation of electric field domains [3] as well as self-sustained oscillations in such structures [4]. While for strongly-coupled superlattices the electronic minibands dominate the electrical transport [5], in weakly-coupled superlattices the transport is due to sequential tunneling from one well to the next. (For a discussion of the appropriate regimes see Refs. [6,7].) This situation has been already regarded in Ref. [8] for tunneling between the lowest level and excited levels in the adjacent well. There the current is driven by the different occupation of the two levels and a maximum of the current occurs when the different level are aligned. Tunneling between equivalent levels at low fields is slightly more complicated, as alignment occurs at zero field, where, of course, the current vanishes. The key point is the treatment of broadening of the states due to scattering which essentially determines the transport. This idea has been exploited to determine scattering rates by studying the transport between two quantum wells [9–11]. In the experiments [10,11] impurity scattering was diminished by the use of remote doping which enabled to study electron-electron scattering rates. In contrast to this we focus on doped superlattices in the present paper. There impurity scattering at the ionized donors is an important scattering process whose impact we will examine in the following. In a previous study [12] a heavily doped sample was

investigated and good agreement with experimental data was found. Here we perform a systematic study of the low-field transport in such structures for different doping densities. We find that the formation of impurity bands [13,14] for low-doped samples causes a strong temperature dependence of the current-field relation which may display a double-peak structure at low fields.

If the superlattice is subjected to an external microwave field, photon-assisted tunneling (PAT) is possible where replica of the resonances are observed at biases which differ from alignment conditions [15–17] by integer multiples of the photon energy. For certain field strengths of the irradiation field absolute negative conductance has been observed experimentally [18,19]. The main features of these experiments could be described qualitatively [18–20] within the standard theory of photon-assisted tunneling [21,22] but modifications due to photon sidebands from a single quantum well [23] have also been suggested to explain the experimental findings. Here we present additional experimental data and show that full quantitative agreement between theory and experiment can be found by a combination of a microscopic transport model with the standard theory of photon-assisted tunneling. This comparison strongly supports our claim that a microscopic treatment of impurity scattering is necessary for a full understanding of transport in low-doped superlattices.

The paper is organized as follows: Our transport model is presented in Section II. In order to understand the generic behavior we give a phenomenological approximation where many features can be seen analytically in Section III. The calculated results for different doping densities are presented in Sections IV and V using different screening models, respectively. Our calculations are compared with two different experiments concerning

a highly-doped and a low-doped sample in section VI. In section VII we consider transport under external irradiation. Finally, we will discuss the general significance of our results.

II. THE MODEL

We consider weakly-coupled semiconductor quantum wells of period d . Then the electrons are essentially localized in the wells and a reasonable basis set of wave functions is given by a product of Wannier functions $\Psi^\nu(z - jd)$, which are maximally localized [24] in well j , and plane waves $e^{i\mathbf{k}\cdot\mathbf{r}}$. The z direction is defined to be the growth direction and \mathbf{k}, \mathbf{r} are vectors within the (x, y) plane. ν denotes the subband within the well. Here we restrict ourselves to the lowest level and omit the index ν in the following and the energy of the lowest level is used as a reference point.

Regarding only next-neighbor coupling T_1 we have the following Hamiltonian (F is the electric field, and $e < 0$ is the charge of the electron):

$$\begin{aligned} \hat{H} = \sum_{j, \mathbf{k}} & \left[(E_k - jeFd) a_j^\dagger(\mathbf{k}) a_j(\mathbf{k}) \right. \\ & \left. + T_1 a_{j+1}^\dagger(\mathbf{k}) a_j(\mathbf{k}) + T_1 a_j^\dagger(\mathbf{k}) a_{j+1}(\mathbf{k}) \right] \\ & + \hat{H}^{\text{scatt}} \end{aligned} \quad (1)$$

with the in-plane kinetic energy $E_k = \hbar^2 k^2 / (2m_w)$, where m_w is the effective mass in the well. a_j and a_j^\dagger are the annihilation and creation operators of electrons in well j , respectively. \hat{H}^{scatt} denotes the contribution due to scattering which is not \mathbf{k} -conserving.

Within the lowest order in the coupling T_1 the current density from the lowest level in well j to the lowest level in well $j+1$ is given by [25]

$$\begin{aligned} J_{j \rightarrow j+1} = & \frac{2e}{A} \sum_{\mathbf{k}} |T_1|^2 \int_{-\infty}^{\infty} \frac{dE}{2\pi\hbar} A_{j+1}(\mathbf{k}, E + eFd) \\ & \times A_j(\mathbf{k}, E) [n_F(E - \mu_j) - n_F(E + eFd - \mu_{j+1})]. \end{aligned} \quad (2)$$

Here e is the electron charge, A is the sample area, μ_j is the local chemical potential in well j measured with respect to the energy of the lowest level. $n_F(\mathcal{E}) = 1/[1 + \exp(\mathcal{E}/k_B T_e)]$, and T_e is the electron temperature. Fd denotes the voltage drop per period d . The spectral function $A(\mathbf{k}, E)$ is calculated for a given intrawell scattering \hat{H}^{scatt} via the retarded self-energy $\Sigma^{\text{ret}}(\mathbf{k}, E)$:

$$A(\mathbf{k}, E) = \frac{-2\text{Im}\{\Sigma^{\text{ret}}(\mathbf{k}, E)\}}{(E - E_k - \text{Re}\{\Sigma^{\text{ret}}\})^2 + (\text{Im}\{\Sigma^{\text{ret}}\})^2}. \quad (3)$$

μ_j is related to the electron density n_j in well j via the relation

$$n_j = \int_{-\infty}^{\infty} dE \rho_j(E) n_F(E - \mu_j) \quad (4)$$

with the density of states

$$\rho_j(E) = \frac{2}{2\pi A} \sum_{\mathbf{k}} A_j(\mathbf{k}, E) \quad (5)$$

where the factor 2 reflects the spin degeneracy.

In our microscopic calculation we proceed as follows: First we determine the coupling T_1 as well as the Wannier functions $\Psi(z - jd)$ for the given superlattice parameters (see Appendix A). Then we calculate the self-energy $\Sigma^{\text{ret}}(\mathbf{k}, E)$ for impurity scattering using the self-consistent single-site approximation shown in Fig. 1. The respective formulas are given in appendix B. The matrix element for impurity scattering is calculated from the Coulomb potential of the individual ionized donors. Screening is treated in two different approaches, the random-phase approximation (RPA) for a free-electron gas and the Thomas-Fermi approximation (TF) using the actual density of states at the Fermi level (see appendix C). Using the calculated spectral functions $A(\mathbf{k}, E)$ the chemical potential is determined by setting $n_j = N_D$ in Eq. (4), where N_D is the doping density per period. Finally the current is calculated from Eq. (2). Note that all quantities used in the calculation are defined by the sample parameters and no fitting parameters are used.

III. PHENOMENOLOGICAL DESCRIPTION

In this section we want to provide some insight into the question how scattering effects the transport. Using a constant self-energy we derive some simple expressions for the current-field relation which will help to understand the full calculations presented in subsequent sections.

As mentioned in the introduction the level broadening essentially determines the transport in the sequential limit. This can be easily seen in the limit of vanishing scattering. Then the spectral functions become δ -functions, $A(\mathbf{k}, E) = 2\pi\delta(E - E_k)$. In this case the current vanishes for $eFd \neq 0$. (In addition further resonances may occur at finite fields, when the lowest level is aligned with higher levels in the neighboring well, which are not considered here). Assuming $eFd \geq 0$ we rewrite Eq. (2) as follows

$$\begin{aligned} J_{j \rightarrow j+1} = & e \frac{T_1^2}{\hbar} \int_{-\infty}^{\infty} dE \langle A_{j+1} \rangle(E, F) \rho_j(E) \\ & \times [n_F(E - \mu_j) - n_F(E + eFd - \mu_{j+1})] \end{aligned} \quad (6)$$

with

$$\langle A_{j+1} \rangle(E, F) = \frac{\int_0^{\infty} dE_k A_j(\mathbf{k}, E) A_{j+1}(\mathbf{k}, E + eFd)}{\int_0^{\infty} dE_k A_j(\mathbf{k}, E)} \quad (7)$$

where we used Eq. (5) and performed the continuum limit. Now let us assume a constant self-energy $\Sigma^{\text{ret}}(\mathbf{k}, E) = -i\Gamma/2$ in Eq. (7) for the sake of simplicity. Then the spectral functions become Lorentzians $A(\mathbf{k}, E) = \Gamma/[(E - E_k)^2 + \Gamma^2/4]$. Extending the lower integration to $-\infty$ we obtain

$$\langle A_{j+1} \rangle = \frac{2\Gamma}{(eFd)^2 + \Gamma^2} \quad (8)$$

which only depends on F . Note that this simple model with a constant self-energy cannot be used in the calculation of the density of states (5) as the integral for the electron density (4) diverges in this case. Therefore we use the free-electron density of states $\rho_j(E) = \rho_0\Theta(E)$ (with $\rho_0 = m/(\pi\hbar^2)$) and obtain for equal chemical potentials $\mu_j = \mu_{j+1} = \mu$:

$$J(F) = e\rho_0 \frac{T_1^2}{\hbar} \frac{2\Gamma}{(eFd)^2 + \Gamma^2} \int_0^{eFd} dE n_F(E - \mu). \quad (9)$$

For low electron temperature and voltage drop ($k_B T_e, eFd \ll \mu$) we find

$$J(F) = e\rho_0 \frac{T_1^2}{\hbar} \frac{2\Gamma eFd}{(eFd)^2 + \Gamma^2} \quad (10)$$

Thus, we recover an ohmic behavior for low fields $eFd \ll \Gamma$, a maximum of $J(F)$ at $eFd = \Gamma$, and negative differential conductivity for $eFd > \Gamma$. Eq. (10) has been essentially used in Refs. [10,11] for the determination of scattering rates Γ/\hbar from tunneling between two two-dimensional electron gases. Similar models using a phenomenological broadening Γ have been applied to the sequential tunneling in superlattices in Refs. [20,26]. The current at the maximum is given by

$$J_{\max} = J \left(\frac{\Gamma}{ed} \right) = e\rho_0 \frac{T_1^2}{\hbar} \quad (11)$$

which is independent of doping, scattering, and temperature in the limit of $\mu \gg eFd, k_B T_e$ considered here.

If $k_B T_e$ becomes of the order of μ the factor $\int_0^{eFd} dE n_F(E - \mu)$ in Eq. (9) is smaller than eFd and we obtain a decrease of the current with temperature. Here we have to take into account the temperature dependence of the chemical potential μ . From Eq. (4) we find $1 + \exp(\mu/k_B T_e) = \exp(n/\rho_0 k_B T_e)$. This gives a zero field conductivity

$$\frac{dJ}{dF}_{|F=0} = \frac{2e^2 \rho_0}{\hbar} \frac{dT_1^2}{\Gamma} \left[1 - \exp \left(-\frac{n}{\rho_0 k_B T_e} \right) \right] \quad (12)$$

which is almost constant for $k_B T_e < n/\rho_0$ and drops as $1/k_B T_e$ for large temperatures as observed experimentally in Ref. [27]. For completeness, we give the result in the high temperature limit ($k_B T_e \gg eFd, n/\rho_0$)

$$J(F) = \frac{en}{k_B T_e} \frac{T_1^2}{\hbar} \frac{2\Gamma eFd}{(eFd)^2 + \Gamma^2} \quad (13)$$

which follows directly from Eq. (9). It is interesting to note, that Eq. (10) is identical to the current-field relation calculated for miniband conduction [28] using a constant scattering time \hbar/Γ for $\mu > 2T_1$ and $k_B T_e = 0$. Equivalently, Eq. (13) has been obtained from miniband transport in the limit $k_B T_e \gg 2T_1, n/\rho_0$ as well [29]. This shows that the models of sequential tunneling and miniband conduction give the same results provided either the electron temperature or the electron density are large.

IV. RESULTS FOR RPA SCREENING

As a model system we choose an $\text{Al}_{0.3}\text{Ga}_{0.7}\text{As-GaAs}$ superlattice with barrier width $b = 10$ nm and well width $w = 10$ nm. We use the conduction band offset 240 meV and the effective masses $m_w = 0.067m_e$ and $m_b = 0.0919m_e$ [30] in the Kronig-Penney model yielding a coupling $T_1 = -0.0116$ meV. We assume δ -doping in the middle of the quantum wells. The interaction with impurities located in different wells is found to be negligibly small. In this section screening is treated within the RPA assuming a free-electron gas.

A. Density of states

In Fig. 2 we show the resulting densities of states for four different doping densities N_D . For high N_D the density of states exhibits a monotonic increase from $\rho = 0$ at $E \leq E_{\min}$ to $\rho \sim \rho_0$ for $E \rightarrow \infty$, where E_{\min} denotes the lowest edge of the density of states. In contrast to this the density of states splits into two parts for small doping: $\rho(E)$ takes finite values in a certain region below $E = 0$, which we will refer to as an impurity band. For higher energies $\rho(E)$ is quite similar to the density of states of the free-electron gas. These results are in good agreement with the findings of Ref. [14]. The onset of the impurity band occurs at slightly larger energies E_{\min} here, as the wavefunctions are less confined due to the spreading into the barrier which was neglected in Ref. [14].

We also marked the positions of the Fermi level E^F (i.e., the chemical potential for $T_e = 0$). For low densities the position is just in the middle of the impurity band, indicating that the impurity band consists of exactly two states per impurity due to the assumed spin degeneracy. (This degeneracy would be lifted if spin-resolved interaction was taken in account, see also appendix B.) For high densities the position of E^F roughly equals the Fermi level of the free-electron gas N_D/ρ_0 . The crossover between these two limits occurs at $N_D \approx 5 \cdot 10^{10}/\text{cm}^2$ where $E^F \approx 0$.

The respective spectral functions are plotted in Fig. 3. For $E = 5$ meV $A(k, E)$ resembles a Lorentzian centered close to $E_k \approx E$. This is the generic behavior of a free

quasiparticle with a finite lifetime due to scattering. The width of the spectral functions is increasing with doping due to the enhanced scattering. We find a full width at half maximum $\Gamma = 0.5$ meV for $N_D \approx 1 \cdot 10^{10}/\text{cm}^2$ and $\Gamma = 5$ meV for $N_D \approx 1 \cdot 10^{11}/\text{cm}^2$, which are in the range of the calculated values of $-2\text{Im}\{\Sigma(\mathbf{k}, E)\}$.

For $E = -5$ meV the spectral functions exhibit a monotonic decrease. For high doping the slope is comparable to the slope at $E = 5$ meV. In contrast to this, the spectral function for $E = 5$ meV and $E = -5$ meV are entirely different for low doping, indicating that two different types of states occur. While the states for $N_D = 10^{10}/\text{cm}^2$ are essentially free-particle states at $E = 5$ meV, they are localized in space for $E = -5$ meV, which is the signature of an impurity band [13].

B. Currents

We calculate the current densities $J_{j \rightarrow j+1}(eFd)$ for different electron temperatures T_e from Eq. (2). The results are shown in Fig. 4. For all temperatures and densities we find an ohmic range for low electric fields and negative differential conductance for high electric fields. Let us first regard the high doping case (a-c), where no impurity bands form and the Fermi level is significantly above $E = 0$. In this case the approximation (9) is justified and indeed we find a maximum at values of eFd which are in the range of calculated values of $\Gamma = -2\text{Im}\{\Sigma^{\text{ret}}(\mathbf{k}, E)\}$. The height is estimated by $J_{\text{max}} = 0.91 \text{A}/\text{cm}^2$ from Eq. (11) which is in good agreement with the full calculation at $T_e = 4$ K. Note that the maximal current is almost independent on the doping in this range. For $N_D = 5 \cdot 10^{11}/\text{cm}^2$ the chemical potential is larger than $k_B T_e$ for all temperatures. Thus, the current is hardly affected by the temperature. In contrast to this the current drops with temperature for lower doping ($N_D = 10^{11}/\text{cm}^2$). All these findings are in good agreement with the phenomenological description using a constant Γ discussed above.

For the low-doped samples (see Figs. 4(e,f)) an entirely new scenario occurs. Here we find two different maxima in the current-field relation whose relative weight is changed by temperature. The reason for this behavior is the presence of impurity bands for these doping levels. For $T_e = 4$ K we find a maximum at $eF_{\text{high}}d \approx 8$ meV. This is due to tunneling from the impurity band to the free states (see Fig. 5(a)). The maximum occurs at the energy where the bottom of the impurity band in one well is aligned with the band edge of the free-electron states in the neighboring well, i.e., $eF_{\text{high}}d \approx |E_{\text{min}}|$. An increasing temperature leads to a transfer of electrons from the impurity band to the free-electron states and consequently the current at $eF_{\text{high}}d$ decreases with increasing T_e . The density of states in the impurity band is much lower than in the free-electron states, and hence the majority of the electrons will be in the free-electron

states for $k_B T_e \gtrsim |E_{\text{min}}|$ (see Fig. 5(b) where the grey scale denotes the relative occupation). The current contribution due to the free-electron states can be understood within the phenomenological constant- Γ approach. There is a maximum at $eF_{\text{low}}d \approx \Gamma$, which coincides with the full width at half maximum of the spectral function at $E = 5$ meV in Fig. 3. The amplitude of this maximum depends on two competing effects: On the one hand the occupation of the free-electron states increases with temperature. On the other hand the Fermi-factor in Eq. (9) strongly decreases with temperature. This explains the calculated behavior, where the peak at $eF_{\text{low}}d$ takes its maximum at intermediate temperatures.

V. RESULTS FOR THOMAS-FERMI SCREENING

The properties related with the formation of impurity bands are sensitive to the actual screening of the interaction [13]. For low doping densities the density of states differs essentially from the free-electron density of states and thus the use of RPA-screening by a free-electron gas is questionable. In order to take this effect into account we use the Thomas-Fermi approximation (TF) with the actual density of states at the Fermi level (see appendix C) in this section. Of course neither the free-electron RPA nor the TF approximation treat the screening entirely correctly, but we hope to obtain some insight into the general features by comparing these two approaches.

In Fig. 6 we show the resulting density of states which is in qualitative agreement with the results of the RPA screening (Fig. 2). For $N_D = 5 \cdot 10^{11}/\text{cm}^2$ the density of states is almost identical while for lower densities some deviations occur. Especially the onset of the impurity band E_{min} is shifted to lower energies for TF-screening. Furthermore the impurity bands extend over a larger energy range and have a lower density of states, so that the total density is conserved. The reason for these deviations lies in the fact that TF-screening is less effective than RPA screening if the actual density of states at the Fermi level is used. Therefore both the binding energy of the impurities as well as the broadening of the states become larger.

This manifests itself in the calculated current densities (see Fig. 7). For high doping (a) the characteristics are almost identical, while for lower doping deviations occur. At first note that the maxima due to tunneling between free-electron states (the maximum for $N_D = 10^{11}/\text{cm}^2$ as well as the maxima F_{low} for $N_D = 2 \cdot 10^{10}/\text{cm}^2$ and $N_D = 10^{10}/\text{cm}^2$) are shifted to the right according to the stronger scattering which increases Γ . At second the peak at F_{high} is shifted to the right compared to Fig. 4. Again we find $eF_{\text{high}}d \approx E_{\text{min}}$ for both densities.

Therefore we conclude that within both approximations for screening the two maxima are determined by specific quantities describing the scattering. $eF_{\text{low}}d$ reflects the average broadening Γ of the free-particle states

and $eF_{\text{high}}d$ is the energy separation between the onset of the impurity band and the free-particle states.

VI. COMPARISON WITH EXPERIMENTS

Previously [12], the formalism was applied for the highly-doped sample ($N_D = 8.75 \cdot 10^{11}/\text{cm}^2$) of Refs. [31,32]. Good quantitative agreement with the experimental data was found, albeit using a barrier width being 10% smaller than the nominal value. (A similar width had been used in the original analysis by the experimentalists as well [32].) The position of the first maximum occurred at $eFd = 13$ meV, which is almost independent of the barrier width (which mainly changes T_1) and in excellent agreement with the experimental finding. The second resonance, as well as the formation of field domains was also studied in Ref. [12], and again good agreement with experimental data was found.

A low-doped superlattice ($N_D = 6 \times 10^9/\text{cm}^2$, $b = 5$ nm, $w = 15$ nm, $A = 8\mu\text{m}^2$) with $N = 10$ wells was used in the experiments of Refs. [18,19] in order to study the transport under strong THz irradiation from a free-electron laser. Additional data for this sample will be given in the following. Without irradiation a broad maximum was found in the range $50 \text{ mV} < U < 100 \text{ mV}$ where the current is almost constant. For $U > 100 \text{ mV}$ domain formation sets in. Dividing by the number of periods ($N = 10$), the maximum extends to $eF_{\text{unirr}}d \approx 10$ meV. In contrast to this, the photon-replica under strong THz-irradiation could be consistently explained by assuming an “instantaneous” current-voltage characteristic [19] with a distinct maximum at $U \approx 20 \text{ mV}$ (i.e., $eF_{\text{irr}}d = 2$ meV).

We calculate the current-field relation for this superlattice using the experimental sample parameters. In order to model the homogeneous doping we use 8 equally spaced δ -doping layers per period. The calculated density of states for both RPA and TF screening is shown in Fig. 8. The density of states resembles the result for low doping found before. Nevertheless we do not find a separation between the impurity band and the free-particle states. The reason is the homogeneous doping: The different impurity positions have different binding energies which smears the impurity band. Again the onset of the impurity band occurs at significantly lower energies within the reduced Thomas-Fermi screening. Both values of $|E_{\text{min}}|$ are smaller than the corresponding values for low doping for the calculation done before (see Figs. 2,6). This is due to the larger well width in the sample: The Wannier-states are less localized and therefore the matrix-element for impurity scattering(B2) as well as the binding energy of the impurity levels is smaller.

The results for the current-field relation are shown in Fig. 9. Again we find two maxima whose relative height changes with temperature. The position of the maximum for low temperatures, $eF_{\text{high}}d$, is almost identical to the

value of $|E_{\text{min}}|$ for both types of screening like in the calculations shown before.

Now we can offer an explanation for the two different maxima occurring in the experiment [18,19] with and without irradiation mentioned above. For low electron temperatures and without irradiation the maximum at $eF_{\text{high}}d$ dominates the transport and thus domain formation sets in at voltages exceeding $U \approx NeF_{\text{high}}d$ where $N = 10$ is the number of wells. If the THz radiation is present the electrons are excited from the impurity band into the free-electron states corresponding to a larger effective electron temperature. Thus, the maximum at $U = NeF_{\text{low}}d$ is dominant, and the photon replicas corresponding to this feature are seen experimentally. The experimental values therefore suggest $eF_{\text{high}}d = 10$ meV and $eF_{\text{low}}d = 2$ meV which is in excellent agreement with the calculation using Thomas-Fermi screening. This indicates that that the RPA using a free electron gas overestimates the screening in low doped samples. The Thomas Fermi approximation with the actual density of states at the Fermi level seems to reproduce the experimental results better in agreement with our argumentation in appendix C. Therefore we will use it in the following for comparison with the experiment.

In Fig. 10 we compare the calculated currents with the experimental current-voltage characteristic without irradiation in a wider range of fields. Here we included the resonance around $eFd \approx 50$ meV between the lowest level and the first excited level as well. The calculation of the corresponding current is completely analogously to Eq. (2), for details see Ref. [7]. Note that there are no fitting parameters involved in the calculation – all quantities including matrix elements and spectral functions are directly calculated for the given sample parameters as outlined above. Let us first focus on the low field region. For $U < 10 \text{ mV}$ the experimental data are in good agreement with the calculated currents for $T_e = 4 \text{ K}$, the experimental lattice temperature. With increasing bias, the experimental data leave the 4K curve and follow the $T_e = 35 \text{ K}$ curve at the plateau between 50 mV and 100 mV. This can be understood by electron heating inside the sample: For a voltage drop of 8 mV per period and a current of $0.6\mu\text{A}$ the Joule heating is $P \approx 10 \text{ pW}$ per electron. In a recent transport experiment a distribution function with $T_e \approx 40 \text{ K}$ was observed [33] for this amount of heating albeit using a sample with higher doping. This shows that the electron temperature strongly deviates from the lattice temperature in the experiment considered in good agreement with our findings. At $U > 100 \text{ mV}$, the homogeneous field distribution becomes unstable, as the region of negative differential conductance is reached and electric field domains form, causing the saw-tooth shape of the characteristic (see Ref. [7] and references cited therein). For $U > 450 \text{ mV}$ one can clearly see the resonance between the lower level and the first excited level in the well which is located 48 meV above the ground level. Again the calculation exhibits two different peaks depending on the electron

temperature due to the different occupation of the impurity bands, although only the high temperature result should be meaningful due to the heating of the carriers. The peak height of around $14\mu\text{A}$ is in excellent agreement with the value of $13.6\mu\text{A}$ found experimentally for our sample. The experimental peak position is located at a higher bias. This may be due to a voltage drop in the receiving contact, where a low-doped spacer layer of $d_{\text{contact}} = 50$ nm thickness exists. If the electric field inside the sample is large, it cannot be screened within the spacer layer and the effective field inside the sample is $U \sim (Nd + d_{\text{contact}})F$ instead of $U = NFd$ as assumed in the figure.

In order to circumvent the problems of electron heating we have investigated the temperature dependence of the zero-bias conductance $G = dI/dU$, where T_e should be equal to the lattice temperature T . The results are shown in Fig. 11 both for our full calculation using TF-screening as well as for spectral functions calculated within the self-consistent Born-approximation (B7) where no impurity bands form. In the latter case G is monotonously decreasing in T as shown in Fig. 11. This can be easily understood within the phenomenological constant- Γ approach(12). However, a different scenario emerges if the electrons occupy impurity bands for low temperatures. Then G is strongly suppressed due to the small values of $A(\mathbf{k}, E)$ for $E < 0$, see Fig. 3. As temperature is increased, more electrons are excited to the free-electron states, and G increases with T until the impurity bands are almost empty at $k_B T \sim |E_{\text{min}}|$. This physical picture is confirmed by the experimental data shown in Fig. 11. At low temperatures the agreement is quantitative, while at intermediate T the theory overestimates G ; this is most likely due to additional scattering processes not included in our calculation, or by the presence of a contact resistance which may limit the experimental conductance.

Thus we may conclude that the results of our calculations are in good agreement with experimental data both for high and low doping. Nevertheless, a direct observation of the two-peak structure is not available so far.

VII. PHOTON-ASSISTED TUNNELING

The standard theory of PAT considers tunneling between two reservoirs between which a dc-voltage ΔU_{dc} is applied. Let us denote the current-voltage characteristic (IV) without irradiation by $I^{\text{dc}}(\Delta U_{\text{dc}})$. Under irradiation an additional ac-bias $U = \Delta U_{\text{ac}} \cos(2\pi\nu t)$ is induced between the reservoirs. Then the time-averaged IV is given by [22]:

$$I^{\text{irr}}(\Delta U_{\text{dc}}) = \sum_{l=-\infty}^{\infty} [J_l(\alpha)]^2 I^{\text{dc}} \left(\Delta U_{\text{dc}} + \frac{lh\nu}{e} \right), \quad (14)$$

where $\alpha = e\Delta U_{\text{ac}}/(h\nu)$ and J_l is the ordinary Bessel function of order l . Thus, the current under irradiation

is given as a sum over the photon replicas $e\Delta U_{\text{dc}} + lh\nu$ where the alignment of the wells is shifted by integer multiples of the photon energy. The great advantage of Eq. (14) is that it expresses all transport properties in terms of $I^{\text{dc}}(\Delta U_{\text{dc}})$. Eq. (14) has been applied to photon-assisted tunneling in weakly-coupled superlattices by identifying $\Delta U_{\text{dc}} = F_{\text{dc}}d$ and $\Delta U_{\text{ac}} = F_{\text{ac}}d$, where F_{ac} is the field component of the microwave field in the growth direction of the superlattice [16,17,19]. Note that Eq. (14) also holds within a miniband model for *strongly-coupled* superlattices [34].

In Refs. [18,20] the $I^{\text{dc}}(eF_{\text{dc}}d)$ curve was calculated phenomenologically and a qualitative agreement with the experimental data could be obtained. To refine the theory we use the results of our microscopic calculation (see Fig. 10) here. As the external irradiation heats the electronic distribution for zero bias as well, we use the curve for $T_e = 35$ K. At this electron temperature about 50% of the electrons are occupying the states in the impurity band. Of course the actual electron distribution may deviate from a Fermi distribution under the strong irradiation. Nevertheless we expect that an effective temperature approach gives a reasonable description of the excited carriers. Further calculations show that the results for $T_e = 30$ K or $T_e = 40$ K do not differ qualitatively. Quantitative agreement between theory (Fig. 12a) and experiment (Fig. 12b) is found for $h\nu = 6.3$ meV (1.5 THz) for different strengths of the laser field. We find a direct tunneling peak at $U_{\text{dir}} = NF_{\text{low}}d \approx 20$ mV and photon replicas at $U \approx U_{\text{dir}} + Nh\nu/e = 83$ mV and $U \approx U_{\text{dir}} + 2Nh\nu/e = 146$ mV. Photon-replicas of the second peak around $NF_{\text{high}}d \approx 100$ mV are less pronounced as this peak is broader. Our calculations show that they become visible if larger photon energies are used. For low bias and high intensities there is a region of absolute negative conductance [18], which we focus on in the following.

In Fig. 12(d) the laser intensity has been tuned such that maximal absolute negative conductance occurred for each of the different laser frequencies. Then we observe a minimum in the current at $U \approx -U_{\text{dir}} + Nh\nu/e$ which is just the first photon replica of the direct tunneling peak on the negative bias side. This replica dominates the current if the direct tunneling channel is suppressed close to the zero of $J_0(\alpha)$ in Eq. (14), i.e., $\alpha \approx 2.4$, as used in the calculation (Fig. 12c). Both the theoretical and experimental results show that absolute negative conductance persists in a wide range of frequencies but becomes less pronounced with decreasing photon energy. In the calculation absolute negative conductance vanishes for $h\nu < 1.8$ meV which is approximately equal to $h\nu \lesssim eF_{\text{low}}d$. The latter relation has been verified by calculations for different samples as well. For $h\nu = 5.3$ meV a smaller value of $\alpha = 2.1$ (thin line) agrees better with the experimental data (in the same sense the value $\alpha = 2.0$ agrees better for $h\nu = 6.3$ meV, compare Fig. 12b). This may be explained as follows: If

strong NDC is present in doped superlattices the homogeneous field distribution becomes unstable and either self-sustained oscillations or stable field domains form [35]. Then the IV deviates from the relation for homogeneous field distribution, where $U = NFd$, and typically shows less pronounced NDC. Therefore maximal negative conductance is observed at a laser field corresponding to a value of $\alpha < 2.4$, where the NDC is weaker and the field distribution is still homogeneous. The presence of an inhomogeneous field distribution could explain the deviations between theory and experiment for $U > 150$ mV as well.

VIII. DISCUSSION

We have investigated the electrical transport in weakly-coupled doped superlattices, where the transport is given by sequential tunneling. Our calculations give negative differential conductance for all doping densities and temperatures at sufficiently large electric fields. This will give rise to instabilities leading to domain formation [36,37] or self-sustained current oscillations [4]. Within the full transport model using Eq. (2) these effects are discussed in Ref. [7].

For high doping $N_D \gtrsim 10^{11}/\text{cm}^2$ or high temperatures $k_B T \gtrsim |E_{\min}|$ the electrons mainly occupy free quasiparticle states. Then the general behavior can be understood within a phenomenological model using a constant self-energy $-i\Gamma/2$. The current exhibits a maximum at $eFd \approx \Gamma$ which can be used to investigate scattering processes. For doped samples impurity scattering is an important scattering process which we considered here. The inclusion of further scattering processes like interface roughness scattering, electron-electron scattering, or phonon scattering will increase Γ and therefore the position of the first peak.

For low-doped samples $N_D \ll 10^{11}/\text{cm}^2$ and low temperatures $k_B T \ll |E_{\min}|$ the presence of impurity bands influences significantly the low-field transport. Then a second maximum at $eF_{\text{high}}d \approx |E_{\min}|$ occurs. This maximum provides a possibility to obtain information about the position of the impurity band. This position depends strongly on the screening as can be seen by comparison of the calculations within RPA and TF. Therefore such experiments could serve as a test on various models for screening. For the sample considered here E_{\min} calculated within the free-particle RPA is too low compared with the experimental onset of domain formation. In contrast the result using TF screening gives excellent agreement with the experimental data. This indicates that screening within the free-particle RPA is too strong for low-doped samples.

Furthermore it would be interesting to see if effects due to spin splitting of the impurity band are visible in experiments. These experiments can be both carried out in doped superlattices as well as in resonant tunneling

between neighboring two-dimensional electron gases in the spirit of Ref. [10,11]. The latter has the advantage that problems due to domain formation in the region of negative differential conductivity are absent. An important aspect in such experiments is the problem of electron heating as the temperature T_e refers to the temperature of the electronic distribution. In order to avoid heating, structures with thick barriers should be used where the Joule heating becomes small.

For external irradiation we have demonstrated both experimentally and theoretically that absolute negative differential conductance persists in a wide range of frequencies $h\nu \gtrsim eF_{\text{low}}d$. The calculated current-voltage characteristics are in excellent quantitative agreement with the experimental data using a microscopically calculated $I^{\text{dc}}(eFd)$ combined with the Tucker formula (14). Recently, the same model has been applied to photon-assisted tunneling in a different sample [38] and quantitative agreement has been achieved as well. This shows that the simple Tucker formula allows for a quantitative description of photon-assisted transport in weakly-coupled superlattices.

ACKNOWLEDGMENTS

We want to thank Ben Hu for stimulating discussions. A.W. and S.Z. acknowledge financial support by the Deutsche Forschungsgemeinschaft. Work performed at the Center for Terahertz Science and Technology was supported by the Office of Naval Research, the Army Research Office and the National Science Foundation.

APPENDIX A: CALCULATION OF THE TRANSITION ELEMENTS

In a superlattice structure the coupling between neighboring wells T_1 is related to the dispersion relation $E(q)$ of the miniband (see [7]) via

$$T_1 = \frac{d}{2\pi} \int_{-\pi/d}^{\pi/d} dq E(q) e^{iqd}. \quad (\text{A1})$$

For a next-neighbor tight-binding model we have $E(q) = -(\Delta/2) \cos(qd)$ and T_1 is equal to a fourth of the miniband width Δ . Here we calculate $E(q)$ for a given superlattice via the Kronig-Penney model for the respective sample parameters. Furthermore we determine the Wannier-functions $\Psi(z - jd)$ localized in well j from the Bloch-functions $\phi_q(z)$, where we choose the phase of the Bloch functions such that the Wannier functions are maximally localized [24]. These Wannier-functions are used for the calculation of the matrix elements for scattering.

APPENDIX B: CALCULATION OF THE SELF-ENERGIES

We assume that the electron density in the conduction band is provided by doping of the superlattice. Thus, scattering at ionized impurities is an important scattering process. In addition there may be interface roughness scattering, phonon scattering, or electron-electron scattering, which we will neglect in the following. For weakly-coupled superlattices, the dominating scattering process occurs within the wells, which are assumed to be identical. Thus, the well index j can be omitted. Scattering at the ionized impurities is described by the Hamiltonian

$$\hat{H}^{\text{scatt}} = \frac{1}{A} \sum_{\mathbf{k}, \mathbf{p}, \alpha} V_\alpha(\mathbf{p}) a^\dagger(\mathbf{k} + \mathbf{p}) a(\mathbf{k}) \quad (\text{B1})$$

where the subscript α denotes the impurity located at the position $(\mathbf{r}_\alpha, z_\alpha)$. The matrix element is calculated with the Wannier functions yielding:

$$\begin{aligned} V_\alpha(\mathbf{p}) &= \int d^2r dz e^{-i\mathbf{p}\cdot\mathbf{r}} \Psi^*(z) \Psi(z) \\ &\quad \times \frac{-e^2}{4\pi\epsilon_s\epsilon_0\sqrt{|\mathbf{r} - \mathbf{r}_\alpha|^2 + (z - z_\alpha)^2}} \\ &= \frac{-e^2}{2\epsilon_s\epsilon_0 p} \int dz \Psi^*(z) \Psi(z) e^{-p|z - z_\alpha|} e^{-i\mathbf{p}\cdot\mathbf{r}_\alpha}. \end{aligned} \quad (\text{B2})$$

Using the bare Coulomb interaction $V_\alpha(\mathbf{p})$ the relevant integrals in the self-energies are divergent. Thus screening is essential for the calculation. We treat screening within the Random-Phase approximation (RPA) of the free-electron gas as well as within an effective Thomas-Fermi approximation(TF) (see appendix C). With the screened impurity potential $V_\alpha^{\text{sc}}(\mathbf{p}) = V_\alpha(\mathbf{p})/\epsilon(\mathbf{p})$ the self-energy is calculated within the self-consistent single-site approximation (shown diagrammatically in Fig. 1) like in Ref. [13]. Then the self-energy contribution from the impurity α is given by

$$\begin{aligned} \Sigma_\alpha(\mathbf{k}, E) &= \frac{1}{A^2} \sum_{\mathbf{k}_1} V_\alpha^{\text{sc}}(\mathbf{k} - \mathbf{k}_1) G(\mathbf{k}_1, E) V_\alpha^{\text{sc}}(\mathbf{k}_1 - \mathbf{k}) \\ &\quad + \frac{1}{A^3} \sum_{\mathbf{k}_1, \mathbf{k}_2} V_\alpha^{\text{sc}}(\mathbf{k} - \mathbf{k}_1) G(\mathbf{k}_1, E) V_\alpha^{\text{sc}}(\mathbf{k}_1 - \mathbf{k}_2) \\ &\quad \times G(\mathbf{k}_2, E) V_\alpha^{\text{sc}}(\mathbf{k}_2 - \mathbf{k}) \\ &\quad + \dots \end{aligned} \quad (\text{B3})$$

where $G(\mathbf{k}, E) = (E - E_k - \Sigma^{\text{ret}}(\mathbf{k}, E))^{-1}$ is the full retarded Green function and

$$\Sigma^{\text{ret}}(\mathbf{k}, E) = \sum_\alpha \Sigma_\alpha(\mathbf{k}, E) \quad (\text{B4})$$

is the sum over all contributions. In case of δ -doping the impurity potentials (B2) from different impurities located in the same well differ only by a phase factor and

the sum over α can be replaced by a multiplication with the number of impurities per layer N_{DA} . Eq. (B3) can be transformed to the self-consistent equation (see, e.g., [13])

$$\begin{aligned} K_\alpha(\mathbf{k}_1, \mathbf{k}, E) &= V_\alpha^{\text{sc}}(\mathbf{k}_1 - \mathbf{k}) \\ &\quad + \frac{1}{A} \sum_{\mathbf{k}_2} V_\alpha^{\text{sc}}(\mathbf{k}_1 - \mathbf{k}_2) G(\mathbf{k}_2, E) K_\alpha(\mathbf{k}_2, \mathbf{k}, E) \end{aligned} \quad (\text{B5})$$

which we solve numerically for a given self-energy function $\Sigma^{\text{ret}}(\mathbf{k}, E)$ entering $G(\mathbf{k}_2, E)$. We parametrize \mathbf{k}_1, \mathbf{k} by E_{k_1}, E_k , and $\phi = \angle(\mathbf{k}_1, \mathbf{k})$ and discretize the resulting equation. This gives a set of linear equations for the components of $K(E_{k_1}, \phi)$ which is solved by matrix inversion. Then the self-energy reads:

$$\Sigma_\alpha(\mathbf{k}, E) = \frac{1}{A^2} \sum_{\mathbf{k}_1} V_\alpha^{\text{sc}}(\mathbf{k}_1 - \mathbf{k}) G(\mathbf{k}_1, E) K_\alpha(\mathbf{k}_1, \mathbf{k}, E). \quad (\text{B6})$$

The equations (B4,B5,B6) have to be solved self-consistently thus determining the self-energy $\Sigma^{\text{ret}}(\mathbf{k}, E)$.

Our single-site-approximations neglects all contributions from crossed diagrams (leading to weak-localization effects, as considered in Ref. [39]) as well as the spin-resolved electron-electron interaction leading to the splitting of the impurity bands (the Mott transition, see e.g. [40]). The latter may become important for very low densities when the impurity bands are narrow. Within this approximation for $\Sigma^{\text{ret}}(\mathbf{k}, E)$ the integral (4) is a well defined quantity, as $\text{Im}\{\Sigma^{\text{ret}}(\mathbf{k}, E)\} = 0$ (and thus $A(\mathbf{k}, E) = 0$ for $E < E_{\min}$).

Finally note that no impurity bands are found within the self-consistent Born approximation

$$\Sigma_\alpha(\mathbf{k}, E) = \frac{1}{A^2} \sum_{\mathbf{k}_1} V_\alpha^{\text{sc}}(\mathbf{k} - \mathbf{k}_1) G(\mathbf{k}_1, E) V_\alpha^{\text{sc}}(\mathbf{k}_1 - \mathbf{k}) \quad (\text{B7})$$

which is just the first diagram from Fig. 1.

APPENDIX C: THE SCREENING

In order to consider screening we have to include the electron-electron interaction given by the Hamiltonian

$$\hat{H}^{ee} = \frac{1}{2A} \sum_{\mathbf{k}, \mathbf{k}', \mathbf{p}} W(\mathbf{p}) a^\dagger(\mathbf{k} + \mathbf{p}) a^\dagger(\mathbf{k}' - \mathbf{p}) a(\mathbf{k}') a(\mathbf{k}). \quad (\text{C1})$$

where the matrix element is calculated via

$$\begin{aligned} W(\mathbf{p}) &= \frac{e^2}{2\epsilon_s\epsilon_0 p} \int dz_1 \int dz_2 \Psi^*(z_1) \Psi^*(z_2) \\ &\quad \times \Psi(z_2) \Psi(z_1) e^{-p|z_1 - z_2|}. \end{aligned} \quad (\text{C2})$$

Within the random-phase approximation (RPA) the screening of the impurity potentials is described by [25]

$$V_\alpha^{\text{RPA}}(\mathbf{p}) = \frac{V_\alpha(\mathbf{p})}{1 - \Pi^0(\mathbf{p}, \omega = 0)W(\mathbf{p})}. \quad (\text{C3})$$

For a free-electron gas the two-dimensional vacuum polarizability $\Pi^0(\mathbf{p}, \omega = 0)$ for $T = 0$ is given by [41]

$$\Pi^0(\mathbf{p}, \omega = 0) = -\rho_0 \left(1 - \Theta(p - 2k_F) \sqrt{1 - 4 \frac{k_F^2}{p^2}} \right). \quad (\text{C4})$$

where $k_F = (2\pi N_D)^{1/2}$ is the Fermi wave-vector.

Actually, the electronic states are affected by the impurity scattering, which may change the density of states dramatically as can be seen from Fig. 2. Now the polarizability $\Pi(p = 0)$ is related to the *actual density of states* at the chemical potential which is significantly lower than ρ_0 . Calculations within the Born-approximation show that the p -dependence of the polarizability becomes weaker and that $\Pi(0)$ decreases with increasing scattering [42,43]. In order to accommodate these trends we make the replacement $\Pi^0(k) \rightarrow \Pi^*(k) = -\rho(E^F)$, given by the calculated density of states of Fig. 2 and the chemical potential at $T = 0$. Then we obtain the screened impurity interaction

$$V_\alpha^{\text{TF}}(\mathbf{p}) = \frac{V_\alpha(\mathbf{p})}{1 + \rho(E^F)W(\mathbf{p})}. \quad (\text{C5})$$

This is equivalent to the Thomas-Fermi approximation for the screening. The same type of screening has been considered in Ref. [13] as well. Of course both ways of including screening are approximations. In a full calculation the scattering has to be treated self-consistently in the calculation of the polarizability. Such a calculation was performed in Ref. [44] for a quantum wire within the restriction of a delta-potential for impurity scattering.

Eq. (C3) only considers screening within the same well. The extension to screening by electrons from neighboring wells is given in section 6 of Ref. [7]. The results are almost indistinguishable for the samples with thick barrier width considered in sections IV and V (see also Ref. [12] for the screened matrix elements). Screening by electrons from neighboring wells becomes more important for a smaller barrier width as used in section VI and VII where the formalism from Ref. [7] was used with the polarization (C4) for RPA and $\Pi^0(k) = -\rho(E^F)$ for the TF case. The temperature dependence of the screening is neglected in all calculations.

- [1] L. Esaki and L. L. Chang, Phys. Rev. Lett. **33**, 495 (1974).
- [2] F. Capasso, K. Mohammed, and A. Y. Cho, Appl. Phys. Lett. **48**, 478 (1986).
- [3] S. H. Kwok, H. T. Grahn, M. Ramsteiner, K. Ploog, F. Prengel, A. Wacker, E. Schöll, S. Murugkar, and R. Merlin, Phys. Rev. B **51**, 9943 (1995).
- [4] J. Kastrup, R. Hey, K. H. Ploog, H. T. Grahn, L. L. Bonilla, M. Kindelan, M. Moscoso, A. Wacker, and J. Galán, Phys. Rev. B **55**, 2476 (1997).
- [5] L. Esaki and R. Tsu, IBM J. Res. Develop. **14**, 61 (1970).
- [6] B. Laikhtman and D. Miller, Phys. Rev. B **48**, 5395 (1993).
- [7] A. Wacker, in *Theory of transport properties of semiconductor nanostructures*, edited by E. Schöll (Chapman and Hall, London, 1997), in print (cond-mat/9701105).
- [8] R. F. Kazarinov and R. A. Suris, Sov. Phys. Semicond. **6**, 120 (1972), [Fiz. Tekh. Poluprov. **6**, 148 (1972)].
- [9] L. Zheng and A. H. MacDonald, Phys. Rev. B **47**, 10619 (1993).
- [10] S. Q. Murphy, J. P. Eisenstein, L. N. Pfeiffer, and K. W. West, Phys. Rev. B **52**, 14825 (1995).
- [11] N. Turner, J. T. Nicholls, E. H. Linfield, K. M. Brown, G. A. C. Jones, and D. A. Ritchie, Phys. Rev. B **54**, 10614 (1996).
- [12] A. Wacker and A.-P. Jauho, Physica Scripta **T69**, 321 (1997).
- [13] A. Gold, J. Serre, and A. Ghazali, Phys. Rev. B **37**, 4589 (1988).
- [14] J. Serre, A. Ghazali, and A. Gold, Phys. Rev. B **39**, 8499 (1989).
- [15] P. S. S. Guimaraes, B. J. Keay, J. P. Kaminski, S. J. Allen, P. F. Hopkins, A. C. Gossard, L. T. Florez, and J. P. Harbison, Phys. Rev. Lett. **70**, 3792 (1993).
- [16] B. J. Keay, S. J. Allen, J. Galán, J. P. Kaminski, K. L. Chapman, A. C. Gossard, U. Bhattacharya, and M. J. M. Rodwell, Phys. Rev. Lett. **75**, 4098 (1995).
- [17] J. Iñarrea and G. Platero, Europhys. Lett. **34**, 43 (1996).
- [18] B. J. Keay, S. Zeuner, S. J. Allen, K. D. Maranowski, A. C. Gossard, U. Bhattacharya, and M. J. M. Rodwell, Phys. Rev. Lett. **75**, 4102 (1995).
- [19] S. Zeuner, B. J. Keay, S. J. Allen, K. D. Maranowski, A. C. Gossard, U. Bhattacharya, and M. J. W. Rodwell, Phys. Rev. B **53**, 1717 (1996).
- [20] G. Platero and R. Aguado, Appl. Phys. Lett. **70**, 3546 (1997).
- [21] P. K. Tien and J. P. Gordon, Phys. Rev. **129**, 647 (1963).
- [22] J. R. Tucker and M. J. Feldman, Rev. Mod. Phys. **57**, 1055 (1985).
- [23] M. Wagner, Phys. Rev. Lett. **76**, 4010 (1996).
- [24] W. Kohn, Phys. Rev. **115**, 809 (1959).
- [25] G. D. Mahan, *Many-Particle Physics* (Plenum, New York, 1990).
- [26] D. Miller and B. Laikhtman, Phys. Rev. B **50**, 18426 (1994).
- [27] G. Brozak, M. Helm, F. DeRosa, C. H. Perry, M. Koza, R. Bhat, and S. J. Allen, Phys. Rev. Lett. **64**, 3163 (1990).
- [28] P. A. Lebwohl and R. Tsu, J. Appl. Phys. **41**, 2664 (1970).

* Present address: Klarastr. 5a, 80636 München, Germany.

[29] A. Y. Shik, Sov. Phys. Semicond. **8**, 1195 (1975), [Fiz. Tekh. Poluprov. **8**, 1841 (1974)].

[30] *Properties of Aluminium Gallium Arsenide*, edited by S. Adachi (INSPEC, London, 1993).

[31] P. Helgesen and T. G. Finstad, in *Proceedings of the 14th Nordic Semiconductor Meeting*, edited by O. Hansen (University of Århus, Århus, 1990), p. 323.

[32] P. Helgesen, T. G. Finstad, and K. Johannessen, J. Appl. Phys. **69**, 2689 (1991).

[33] W. Hilber, M. Helm, K. Alavi, and R. N. Pathak, Appl. Phys. Lett. **69**, 2528 (1996).

[34] A. A. Ignatov, E. Schomburg, J. Grenzer, K. F. Renk, and E. P. Dodin, Z. Phys. B **98**, 187 (1995).

[35] A. Wacker, M. Moscoso, M. Kindelan, and L. L. Bonilla, Phys. Rev. B **55**, 2466 (1997).

[36] F. Prengel, A. Wacker, and E. Schöll, Phys. Rev. B **50**, 1705 (1994), ibid **52**, 11518 (1995).

[37] L. L. Bonilla, J. Galán, J. A. Cuesta, F. C. Martínez, and J. M. Molera, Phys. Rev. B **50**, 8644 (1994).

[38] A. Wacker and A.-P. Jauho, phys. status solidi (b) , in print.

[39] W. Szott, C. Jedrzejek, and W. P. Kirk, Phys. Rev. B **45**, 3565 (1992).

[40] B. I. Shklovskii and A. L. Efros, *Electronic Properties of Doped Semiconductors* (Springer, Berlin, 1984).

[41] F. Stern, Phys. Rev. Lett. **18**, 546 (1967).

[42] T. Ando, J. Phys. Soc. Jpn. **51**, 3215 (1982).

[43] S. Das Sarma, Phys. Rev. Lett. **50**, 211 (1983).

[44] B. Y. Hu and S. Das Sarma, Phys. Rev. B **48**, 5469 (1993).

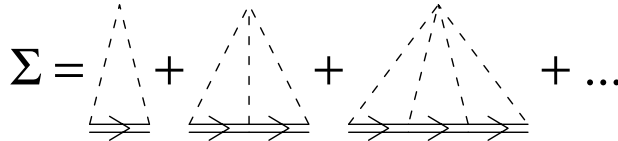


FIG. 1. The self-consistent single-site approximation. The dashed lines indicate impurity potentials and the double lines denote the full Green-function

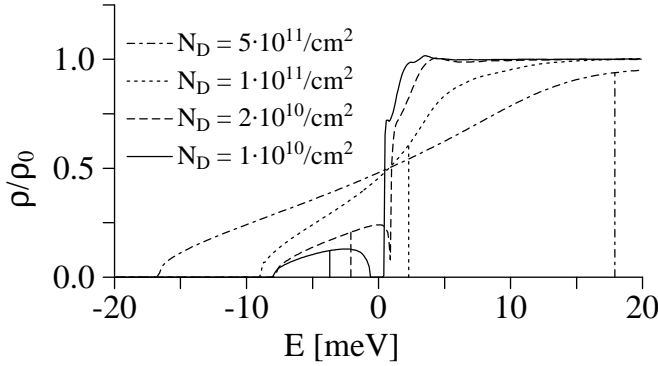


FIG. 2. Calculated density of states in units of the 2D free carrier density ρ_0 using RPA screening. The vertical lines indicate the position of the chemical potential for $T = 0$ at the respective doping densities.

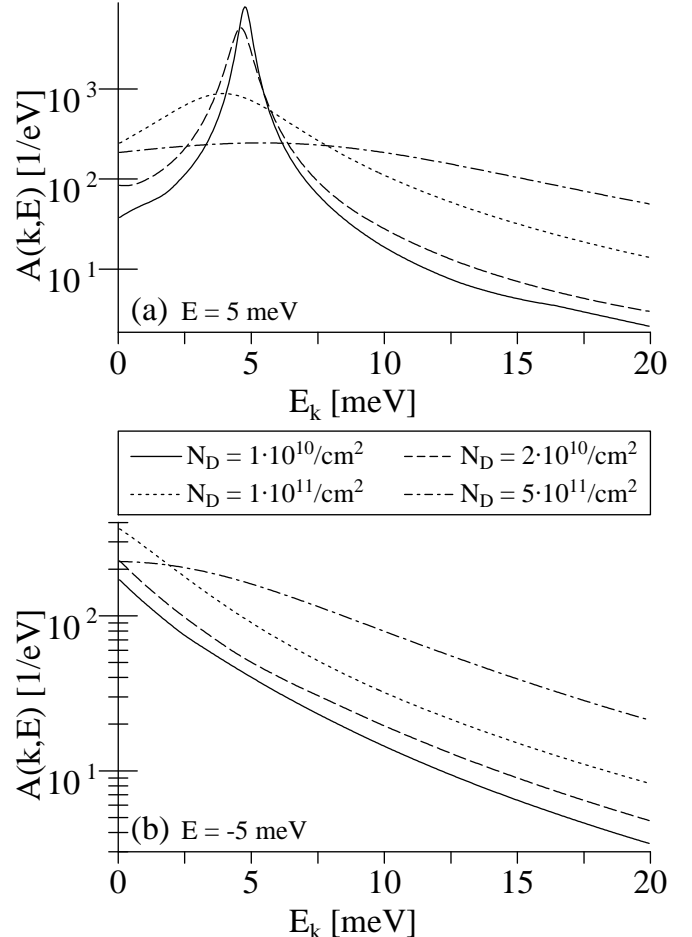


FIG. 3. Calculated spectral functions $A(E, k)$ versus $E_k = \hbar^2 k^2 / 2m$ using RPA screening for different doping densities at $E = 5$ meV (a) and $E = -5$ meV (b).

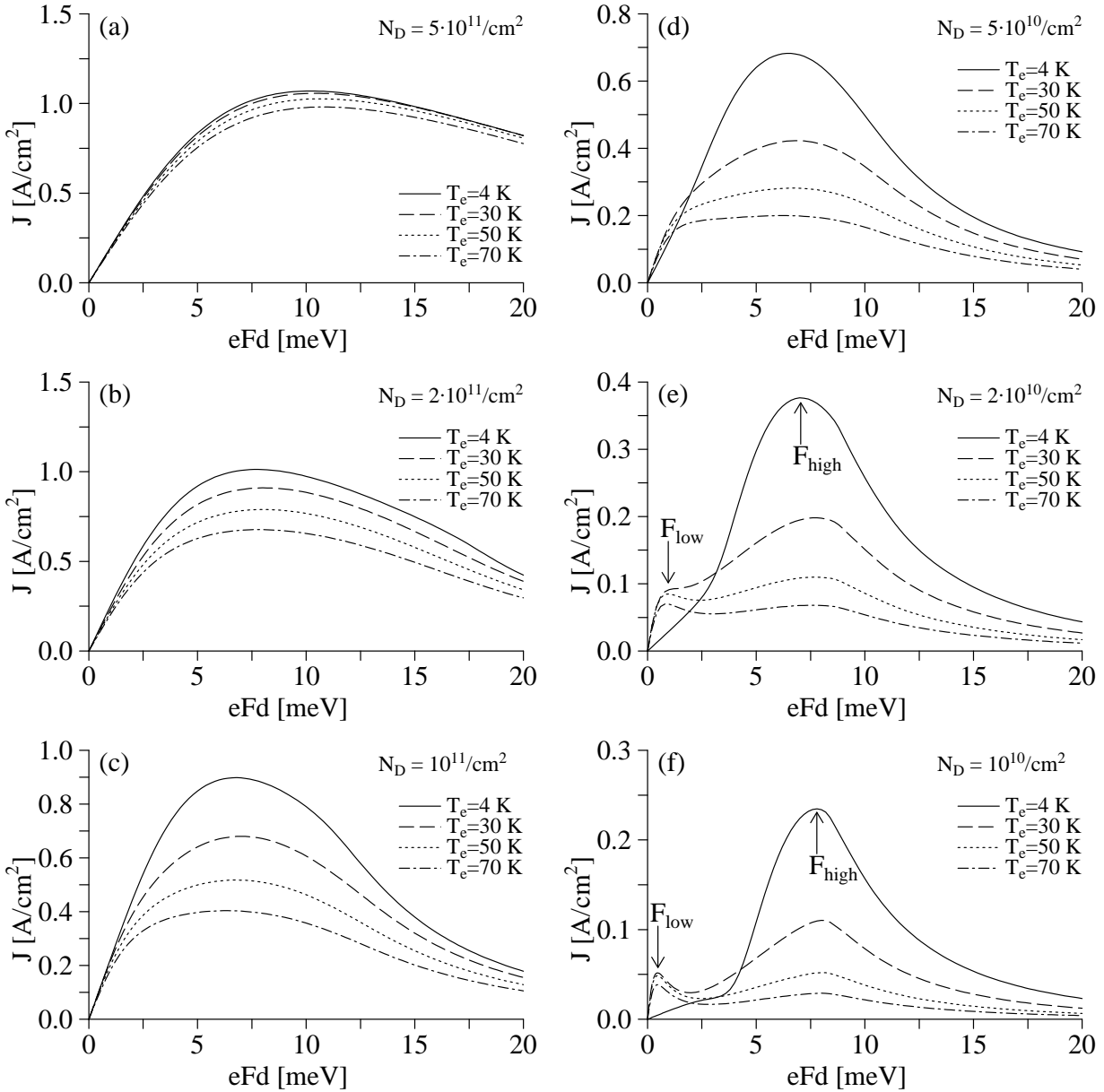


FIG. 4. Calculated temperature dependence of the current-field relations for different doping densities. The screening is treated within the RPA.

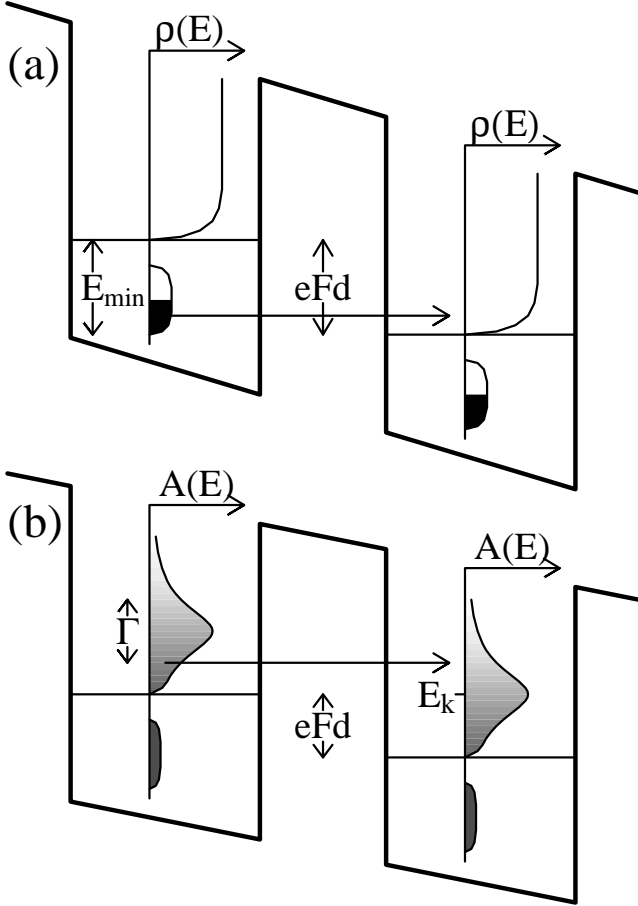


FIG. 5. Explanation of the two different current maxima within a sketch of the conduction band profile: (a) For low temperatures the electrons occupy the impurity band (black area). As these states exhibit a flat spectral function (see Fig. 3(b)) they contain contributions from essentially all \mathbf{k} -vectors and thus tunneling into the free-particle states is possible at all energies. Maximal current is found when all states from the impurity band can tunnel into the free-particle states, i.e., $eFd \approx |E_{\min}|$. (b) For high temperatures the electrons occupy the free-electron states as well (the grey scale indicates the occupation given by the Fermi-function). The spectral function $A(\mathbf{k}, E)$ of such a free-electron state with given wave vector \mathbf{k} is peaked around $E = E_k$ as shown in the figure. Due to \mathbf{k} -conservation tunneling can only take place if the spectral functions for the same \mathbf{k} of both wells overlap. On the other hand a net current is caused by the difference in occupation. This competition results in a current maximum for $eFd \approx \Gamma$ as shown in section III.

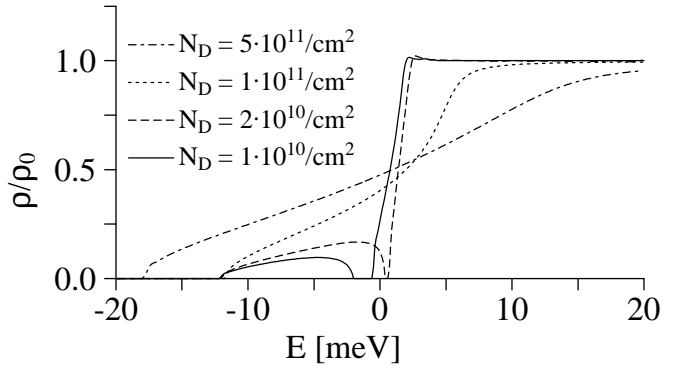


FIG. 6. Calculated density of states in units of the 2D free carrier density ρ_0 using Thomas-Fermi screening for different doping densities.

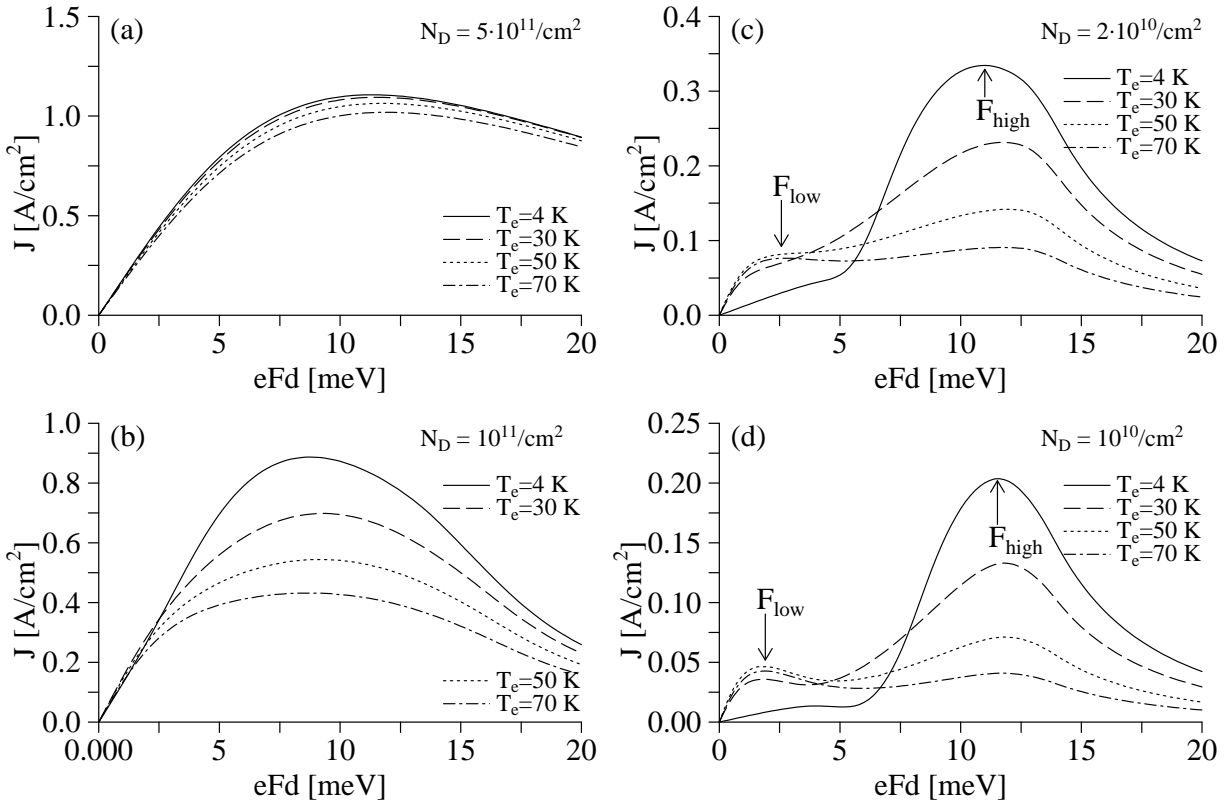


FIG. 7. Calculated temperature dependence of the current-field relations for different doping densities using TF screening.

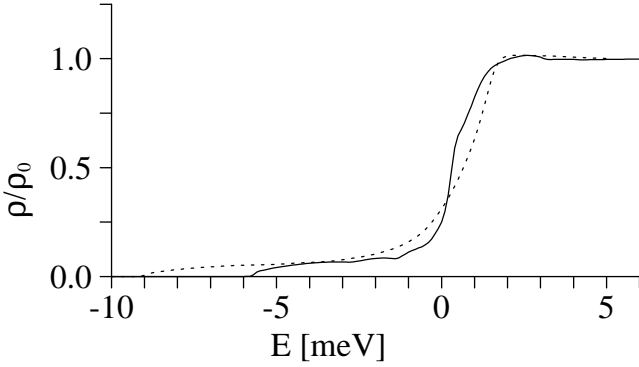


FIG. 8. Calculated density of states for the sample parameters of Ref. [18,19] using RPA screening (full line) and TF screening (dashed line).

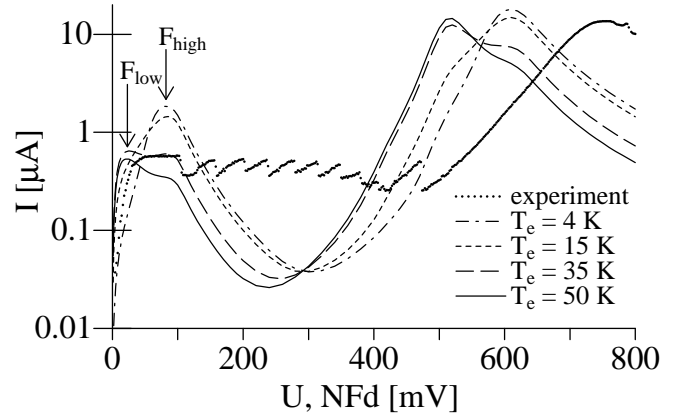


FIG. 10. Experimental current-voltage characteristic without external irradiation together with calculations for different electron temperatures. In the calculation we estimate the bias by NFd assuming a homogeneous field distribution and neglecting potential drops in the contact regions.

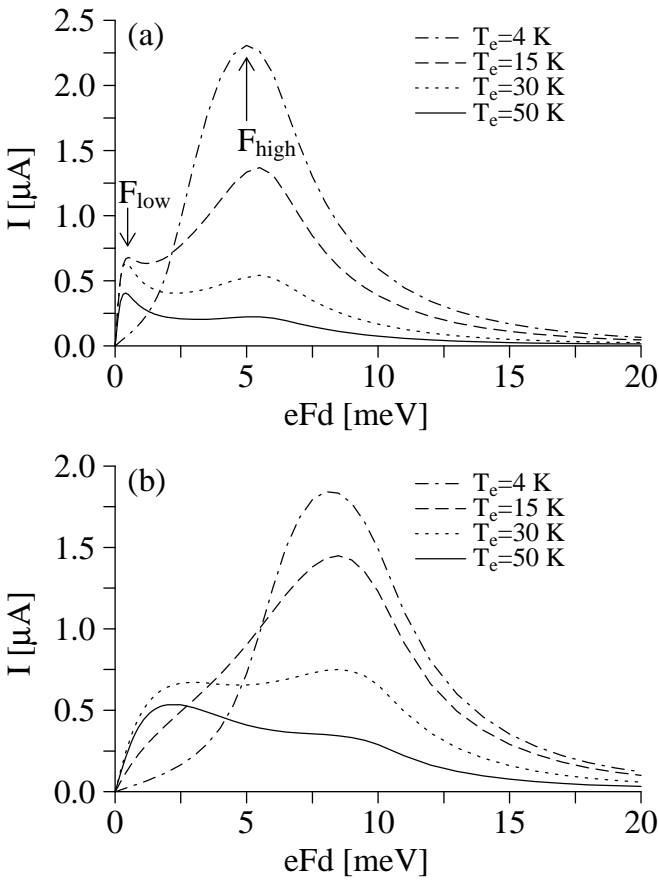


FIG. 9. Calculated temperature dependence of the current-field relations for the sample of Ref. [18,19]. The screening is treated within the RPA (a) and within the Thomas-Fermi approximation (b).

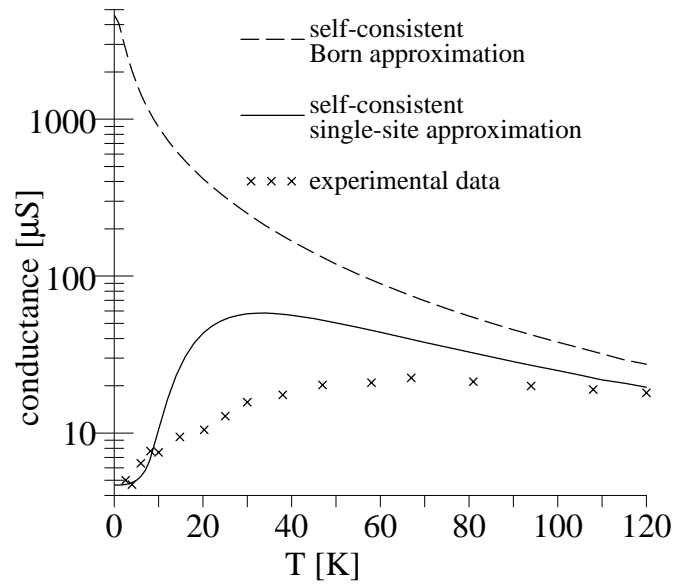


FIG. 11. Temperature dependence of the zero-bias conductance for the sample of Refs. [18,19]. Full line: Calculation using spectral functions from the single-site approximation and TF screening, dashed line: Calculation using spectral functions from the self-consistent Born-approximation, crosses: experimental data

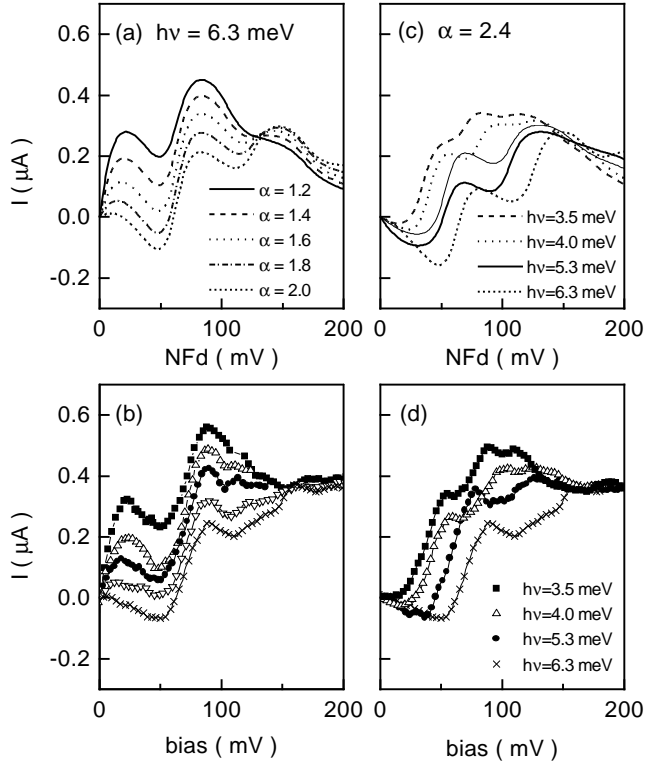


FIG. 12. Current-voltage characteristics under irradiation. a) Theoretical results for $h\nu = 6.3$ meV and different field strength $eF_{ac}d = \alpha h\nu$ of the irradiation. b) Experimental results for $h\nu = 6.3$ meV and different laser intensities increasing from the top to the bottom. The actual values F_{ac} inside the sample are not accessible. c) Theoretical results for $\alpha = 2.4$ and different photon energies. The thin line depicts $h\nu = 5.3$ meV and $\alpha = 2.1$. d) Experimental results for different photon energies. The laser intensity was tuned to give maximum negative conductance.